RESEARCH ARTICLE

ADVANCED OPTICAL MATERIALS
www.advopticalmat.de

High-Index and Low-Loss Topological Insulators for Mid-Infrared Nanophotonics: Bismuth and Antimony Chalcogenides

*Sergey G. Menabde, Jacob T. Heiden, Vladimir A. Zenin, N. Asger Mortensen, and Min Seok Jang**

Topological insulators generally have dielectric bulk and conductive surface states. Consequently, some of these materials are shown to support polaritonic modes at visible and THz frequencies. At the same time, the optical properties of topological insulators in the mid-infrared (mid-IR) remain poorly investigated. Here, near-field imaging is employed to probe the mid-IR response from the exfoliated flakes of bismuth (Bi)/selenide (Se)/telluride (Te)/antimony (Sb) crystals with varying stoichiometry – Bi_2Se_3, Bi_2Te_2Se, and $Bi_{1.5}Sb_{0.5}Te_{1.7}Se_{1.3}$ – in pristine form as well as covered by thin flakes of hexagonal boron nitride (hBN) is employed. Contrary to theoretical expectations, all three materials exhibit a dielectric response with a high refractive index and with a loss below the experimental detection limit. Particularly, the near-field mapping of propagating phonon-polaritons in hBN demonstrates that all three van der Waals crystals with different stoichiometry act as a practically lossless dielectric substrate with an ultra-high refractive index of up to 7.5 in Bi_2Te_2Se. Such a unique dielectric crystal will be of great advantage for numerous nanophotonic applications in the mid-IR.

1. Introduction

Strong spin-orbit coupling in topological insulators (TIs) leads to an electronic band inversion and the topological Dirac surface states in the bandgap.[1,2] These surface states are chiral and thus topologically protected from back-scattering by the time-reversal symmetry.[3] Therefore, charge carriers in surface states are free to move parallel to the surface and conduct current, while the insulating bulk remains dielectric. This particular property of TIs prompted significant interest from the photonics community as it promises exotic electrodynamic phenomena across a wide frequency spectrum. Furthermore, these materials provide a wide range of bandgap energies, promising broadband photodetection from UV to THz frequencies.[4,5]

The conductive surface state provides a condition for the manifestation of surface plasmons at optical frequencies in bismuth and antimony chalcogenides.[6,7] For example, a particularly strong plasmonic response in visible and ultraviolet spectra has been reported in $Bi_{1.5}Sb_{0.5}Te_{1.8}Se_{1.2}$ (BSTS).[8,9] Propagating surface plasmons in the visible spectrum have been directly observed with the scattering-type scanning near-field optical microscope (s-SNOM)[10] in Bi_2Te_2Se (BTS).[11] On the other hand, bulk Bi_2Se_3 (BS) is a polar dielectric and was predicted to support hyperbolic phonon-polaritons (HPP) in the THz regime[12] where its surface supports Dirac plasmons.[13] Later, the existence of the THz plasmon-phonon-polaritons in BS was confirmed by far-field experiments.[14–16] THz near-field imaging has been recently used to demonstrate the existence of the plasmon-phonon-polaritons in both BS[17,18] and BTS.[17]

According to the theoretical models developed for these three TI materials (BS, BTS, and BSTS), all of them are expected to have a high-index low-loss dielectric bulk and a conductive surface at mid-infrared (IR) frequencies.[6,7] Other topological insulators such as Bi_2Te_3[19–22] and Bi:Sb:Te family[23,24] are known to have a very high refractive index, but their bulk is lossy in the mid-IR.[20,22]

Motivated by this, we aim to study the interaction between the highly-confined HPP in hexagonal boron nitride (hBN) and the topological surface states in BS, BTS, and BSTS of optimized chemical composition $Bi_{1.5}Sb_{0.5}Te_{1.7}Se_{1.3}$. To this end, we place thin (30–115 nm-thick) exfoliated flakes of hBN on top of the exfoliated TI crystals and obtain near-field images of propagating HPP using s-SNOM. Surprisingly, the measured HPP dispersion

S. G. Menabde, J. T. Heiden, M. S. Jang
School of Electrical Engineering
Korea Advanced Institute of Science and Technology
Daejeon 34141, South Korea
E-mail: jang.minseok@kaist.ac.kr
V. A. Zenin
Center for Nano Optics
University of Southern Denmark
Odense DK-5230, Denmark
N. A. Mortensen
POLIMA – Center for Polariton-driven Light-Matter Interactions
University of Southern Denmark
Odense DK-5230, Denmark
N. A. Mortensen
Danish Institute for Advanced Study
University of Southern Denmark
Odense DK-5230, Denmark

The ORCID identification number(s) for the author(s) of this article can be found under https://doi.org/10.1002/adom.202302797

DOI: 10.1002/adom.202302797

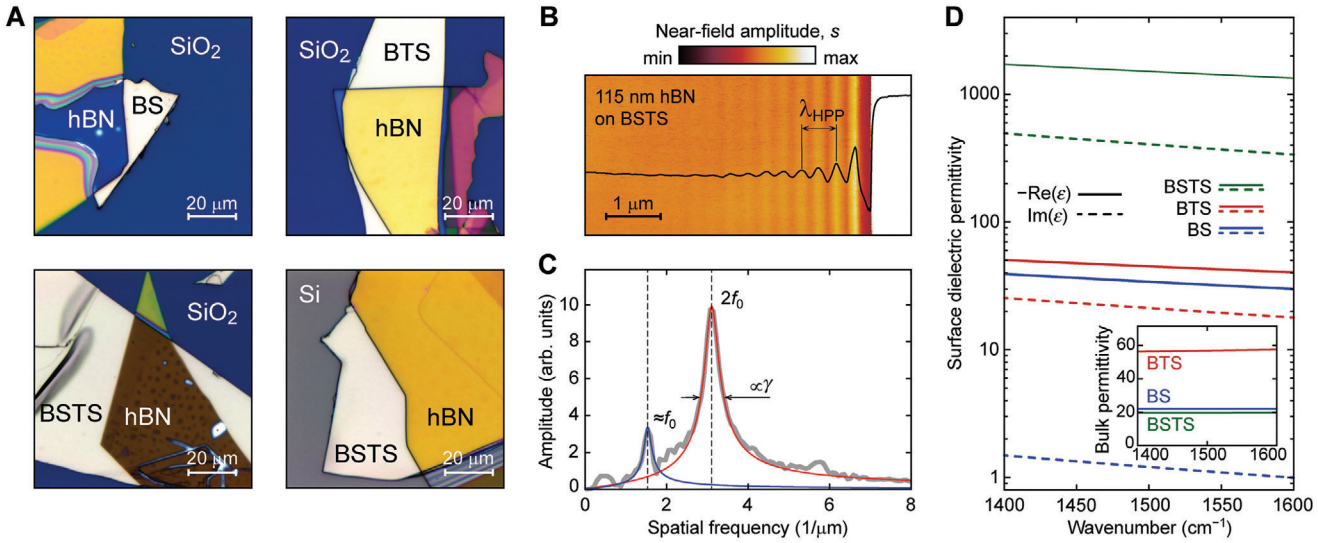

Figure 1. A) Optical microscope image of hBN flakes placed of the TI flakes: 52, 113, and 30 nm-thick hBN on 275, 145, and 160 nm-thick BS, BTS, and BSTS, respectively, on Si/SiO2 wafer; and 115 nm-thick hBN on 200 nm-thick BSTS on Si wafer. B) Near-field amplitude at 1500 cm^{-1} mapped over the hBN edge in the hBN/BSTS/Si sample. Profile of the near-field interference fringes (black curve) reveals the wavelength of the propagating phonon-polaritons. C) Fourier spectrum of the interference profile in (B), fitted by the Lorentzian-like spectrum of a damped oscillator for the nanotip-launched HPP (red) and the edge-launched HPP (blue). D) Modelled 2D Drude permittivity of the topological surface layer in TI crystals at frequencies around the second Reststrahlen band of hBN. Inset: bulk dielectric permittivity according to the Tauc–Lorentz model for BTS and BSTS and the approximation for BS.

does not reveal any unambiguous signatures of the conductive surface states in any of the three materials. To confirm this observation, we analyze the complex near-field signal over the samples with hBN and across bare TI flakes on a silicon (Si) substrate. Again, the multifaceted near-field analysis does not exhibit any clear features of the conductive surface states in the TI crystals. At the same time, all experiments demonstrate the ultra-high refractive index and practically lossless nature of the three TI crystals in the tested mid-IR range (950–1600 cm^{-1}). Despite the possible existence of conductive surface states, our results suggest that in practice BS, BTS, and BSTS can be used as low-loss and ultra-high-index van der Waals dielectrics for numerous mid-IR applications.[25,26]

This discovery is particularly important in the context of the rapidly advancing field of mid-IR hyperbolic polaritons in van der Waals crystals[27] which recently demonstrated a plethora of new phenomena such as ghost and sheer phonon-polaritons in low-symmetry crystals,[28] nanolight manipulation in twisted van der Waals crystals,[29] and electrical manipulation of hybrid plasmon-phonon-polaritons in van der Waals heterostructures.[30] All these new applications may greatly benefit from low-loss and ultra-high-index van der Waals dielectrics which would provide polaritons with significantly increased momenta without introducing additional loss.

2. Results and Discussion

Optical images of exfoliated TI flakes with transferred hBN flakes on top are shown in **Figure** 1A. During the s-SNOM experiments, an atomic-force microscope (AFM) nanotip launches HPP waves that interfere with the same modes reflected at the hBN edge and form a near-field interference pattern with a period of $\lambda_{HPP}/2$, where λ_{HPP} is the HPP wavelength.[31–33] Figure 1B shows an example of such an interference pattern imaged at 1500 cm^{-1} in the 115 nm-thick hBN on a 200 nm-thick BSTS flake. The near-field amplitude s is proportional to the amplitude of the out-of-plane component of the electric field, thus the interference pattern maps the electric field's amplitude of propagating polaritons (black curve in Figure 1B). Assuming that the interference profile has the form of a damped harmonic oscillator, $s(x) = Ae^{-\gamma x}\cos(f_0 x)$, its Fourier spectrum can be accurately fitted with a Lorentzian-like profile which provides the polariton momentum $k = 2\pi/\lambda_{HPP} = 2\pi f_0$ and the decay constant γ, as illustrated in Figure 1C.

Note that the γ extracted for the tip-launched polaritons with diverging wavefront (red curve in Figure 1C) exceeds the actual decay constant of the HPP. In principle, the actual HPP damping can be estimated from the interference pattern formed by the edge-launched modes and the s-SNOM excitation beam[32] (blue curve in Figure 1C). However, thin hBN edges have a small scattering cross-section and typically launch HPP less efficiently compared to the sharp metalized nanotip.[31] Therefore, in this work, we use the consistently strong signal from the tip-launched polaritons to extract HPP momentum and analyze the relative propagation loss.

For the analytical investigation, we employ the Drude model to describe the dielectric permittivity of the surface layer of finite thickness ≈1.5 nm[6,8,9,11,34,35] and the Tauc–Lorentz model for the bulk BTS and BSTS.[8,11] Among the three materials, BSTS is predicted to have the highest surface conductivity comparable to that of a noble metal (Figure 1D). At the same time, Ohmic loss in BS is predicted to be more than two orders of magnitude lower than in BSTS (Figure 1D). Notably, the predicted permittivity of bulk BTS is as high as 57, while being practically

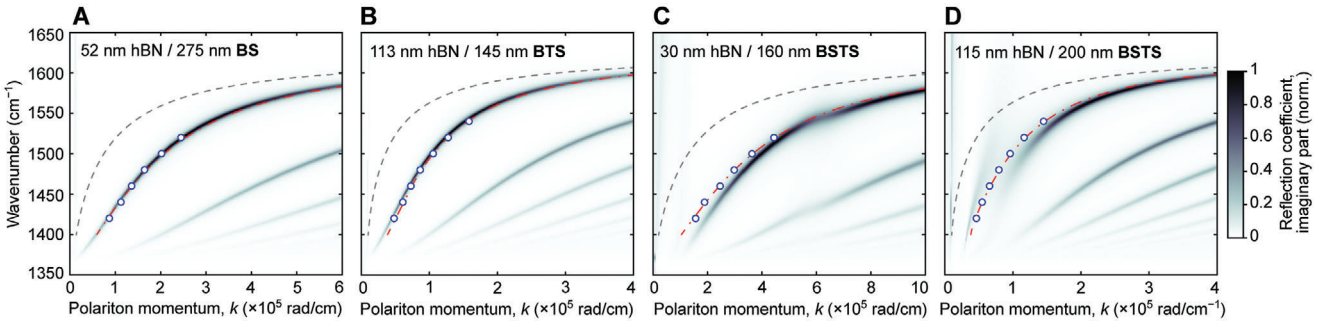

Figure 2. Dispersion of HPP in the samples shown in Figure 1: calculated assuming TI crystals with conductive surface layers (color map), without the surface layers (red dash-dotted), and experimentally measured (data points). A–C) Samples on Si/SiO_2 wafer. D) Sample on Si wafer. Also shown is HPP dispersion in a free-standing hBN of corresponding thickness (grey dashed).

dispersionless and lossless throughout the mid-IR spectrum of interest (inset in Figure 1D). The broadband dispersionless and lossless behaviors are qualitatively reflecting the principle of causality and Kramers–Kronig relations. The dielectric function of hBN is retrieved from Raman spectroscopy and near-field probing of a sample on a Si substrate. A detailed description of the employed models is provided in the Supplement.

2.1. Dispersion and Loss of Phonon-Polaritons in Heterostructures with hBN

The dispersion of eigenmodes in a continuous multilayer structure can be revealed by mapping the imaginary part of the reflection coefficient in momentum space, calculated by a generalized transfer-matrix method.[36] In addition, the transfer-matrix method provides the exact dispersion solution when formulated as an eigenvalue problem.[32]

Figure 2A–D summarizes the analytically calculated and measured dispersion of HPP in hBN for corresponding samples shown in Figure 1A. The dispersion is calculated assuming a continuous multilayer structure for three cases: with the conductive surface layers (color map), without the surface layers (exact solution shown by red dash-dotted line), and for the suspended hBN (exact solution shown by grey dashed line). No additional fitting parameters are used to plot analytical dispersions in Figure 2. The modeled permittivity of surface layers in BS and BTS appears to be too low to cause any significant perturbation of the HPP dispersion (Figure 2A,B) due to the large momentum mismatch between the HPP and the surface plasmons in BS and BTS (Figure S3A,B, Supporting Information). However, much more conductive BSTS surfaces are expected to support plasmonic modes with much smaller momentum that can hybridize with the HPP and significantly perturb the dispersion (color map in Figure 2C,D; Figures S3C and S4, Supporting Information). Therefore, we studied three samples with 30, 86, and 115 nm-thick hBN on BSTS to probe different regions of the momentum space (dispersion for 86 nm-thick hBN is shown in Figure S5, Supporting Information).

As expected, the HPP in all samples is significantly more confined compared to the free-standing hBN due to the high-index TI substrates. To our surprise, however, experimental results in every case are explained by the analytical dispersion that neglects possible contributions from the theoretically anticipated conductive surface layers. Further discussion is focused on investigating this unexpected observation.

To commence, we note that any conductive surface states are expected to cause a slightly higher propagation loss of HPP compared to hBN on a low-loss substrate, thus also potentially providing a means for its experimental detection. As a figure of merit (FOM) for the HPP loss, we use the ratio $k/2\pi\gamma$ that gives a normalized propagation length in units of polariton wavelengths. Since TI materials are van der Waals crystals, we selected flakes with flat surfaces (by using dark-field microscopy for inspection) to minimize the scattering-mediated loss. **Figure 3** shows the HPP FOM in hBN on TI crystals and on a Si wafer which is practically lossless and dispersionless at the frequencies of interest.[37] In notable agreement, the FOM on TI flakes is very similar to that on the Si wafer, indicating the absence of additional loss.

Summarizing the near-field study of the propagating HPP in hBN at 1420–1540 cm^{-1}, we conclude that the investigated TI materials behave as low-loss dielectrics with the refractive index correctly predicted by the Tauc–Lorentz model. At the same time, any interaction between the conductive surface states and HPP

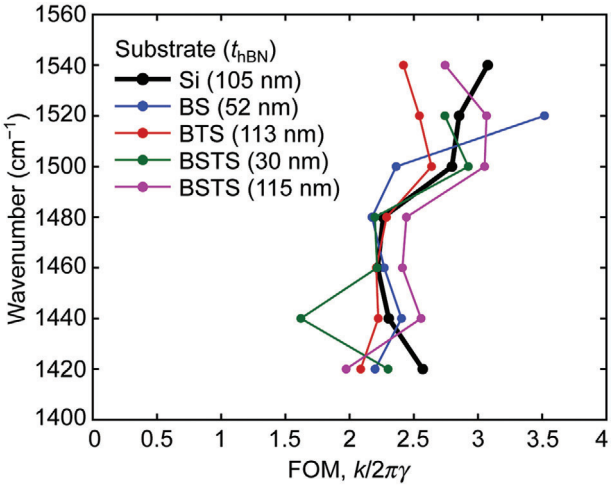

Figure 3. Figure of merit for the HPP propagation loss in the samples shown in Figure 1A (colors) and that in the hBN on a silicon substrate (black).

remains undetected even when polaritons hybridization is expected in BSTS.

2.2. Near-Field Phase Analysis

To further investigate our intriguing findings, we analyze the complex-valued s-SNOM signal $\sigma = se^{i\varphi}$ over different areas of the samples far away from edges, which carries information about the local material properties under the nanotip. The amplitude s is proportional to the near-field reflectivity of the material, and its phase φ has been associated with the loss in the sample.[38] At the same time, the background signal in s-SNOM (i.e., not from the near-field interaction) is suppressed by demodulation of σ at higher-order harmonics of the AFM tapping amplitude.[39] Due to the highly nonlinear dependency of σ on the tip-sample distance, the higher-order harmonics $\sigma_{n>2}$ probe the near-field within a smaller volume under the tip,[40–42] as schematically shown in **Figure** 4A. Hence their phase $\varphi_{n>2}$ corresponds to the electromagnetic loss in a different volume, depending on n. The phase ambiguity caused by the random but constant term from the reference arm of the SNOM's interferometer can be eliminated by considering the phase difference $\varphi_{n+1} - \varphi_n$. Particularly, it has been demonstrated that $\varphi_{n+1} - \varphi_n > 0$ in the presence of a thin layer of lossy material on top of the sample, and $\varphi_{n+1} - \varphi_n = 0$ when the sample is lossless.[40–42] Therefore, the presence of the Drude layer (black dashed line in Figure 4a) would lead to $\varphi_{n+1} - \varphi_n > 0$ even if the bulk would be lossless. Here, we apply this technique in an attempt to detect the elusive surface state in BSTS.

Figure 4B shows the map of $\varphi_4 - \varphi_3$ over the hBN edge on BSTS at 1500 cm^{-1} in the two samples with hBN thickness t_{hBN} = 30 and 115 nm. We note that the thickness of BSTS in both samples is larger than 150 nm, which exceeds the near-field probing depth for $n > 2$,[40,43] thus isolating the signal from the different substrates under BSTS. Corresponding spatial profiles of $\varphi_4 - \varphi_3$ are shown in Figure 4C. First, $\varphi_4 - \varphi_3 \approx 0.4°$ and –0.5° over the BSTS in the sample with thinner and thicker hBN, respectively. Second, $\varphi_4 - \varphi_3 > 0$ far from the hBN edge (where the HPP interference does not contribute to near-field signal), and is larger in the sample with thinner hBN as expected from a thinner absorbing layer.[40] This concludes that the hBN is responsible for the near-field loss probed by φ_4 and φ_3, while BSTS is practically lossless.

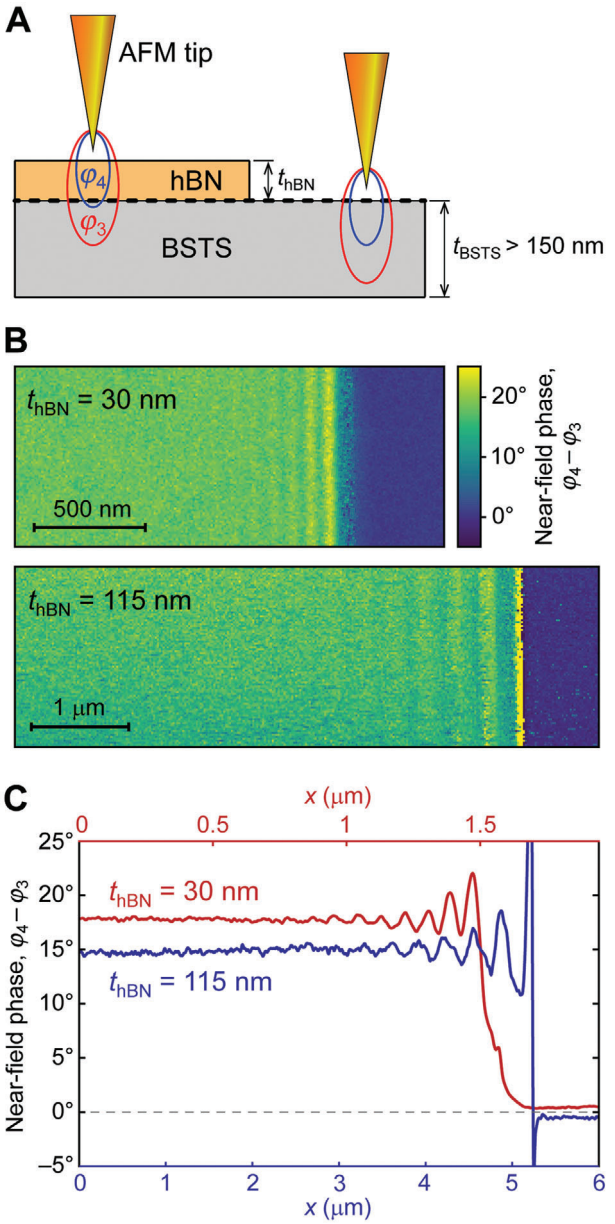

Figure 4. A) Schematic demonstration of how the higher-order harmonics of the near-field signal probe the smaller volume under the nanotip in the sample. This leads to $\varphi_{n+1} - \varphi_n > 0$ over the lossy sample areas, including the hypothetical case when only the surface state is lossy (dashed black line). B) Maps of $\varphi_4 - \varphi_3$ over the hBN edge on BSTS in the two different samples mapped at 1500 cm^{-1}. C) Spatial profiles of $\varphi_4 - \varphi_3$ averaged across the scan areas shown in (B).

2.3. Near-Field Analysis on Si Substrate

Finally, we conduct near-field contrast analysis for all three (bare) TI materials on Si substrate at two frequencies 950 and 1600 cm^{-1}. Since Si can be considered practically lossless across the mid-IR spectrum, the imaginary part of the near-field contrast $\eta = \sigma/\sigma_{Si}$ over the TI flakes would reveal the presence of any loss.

Figure 5 summarizes the near-field contrast of the three TI flakes at 950 cm^{-1} (data at 1600 cm^{-1} is provided in the Supporting Information Figure S6, Supporting Information). The real part of the near-field contrast Re $(\eta) = s/s_{Si}$ (Figure 5A) is proportional to the tip polarizability, which is a function of dielectric permittivity.[40] In agreement with the Tauc–Lorentz model, s/s_{Si} is significantly higher over BTS, resulting from the very high bulk permittivity ($\epsilon_{BTS} \approx 57$), while $s_{BS}/s_{Si} \approx 1$ indicates that the permittivity of BS is approximately equal to that of Si ($\epsilon_{Si} = 12.04 + 5i \times 10^{-4}$ at 950 cm^{-1}[37]). In principle, near-field contrast can be used to extract the dielectric function of an unknown material by probing the samples of different thicknesses.[43–45] However, this task is prohibitively complex and is out of the scope of this work. The normalized phase (Figure 5B) does not exhibit any clear contrast

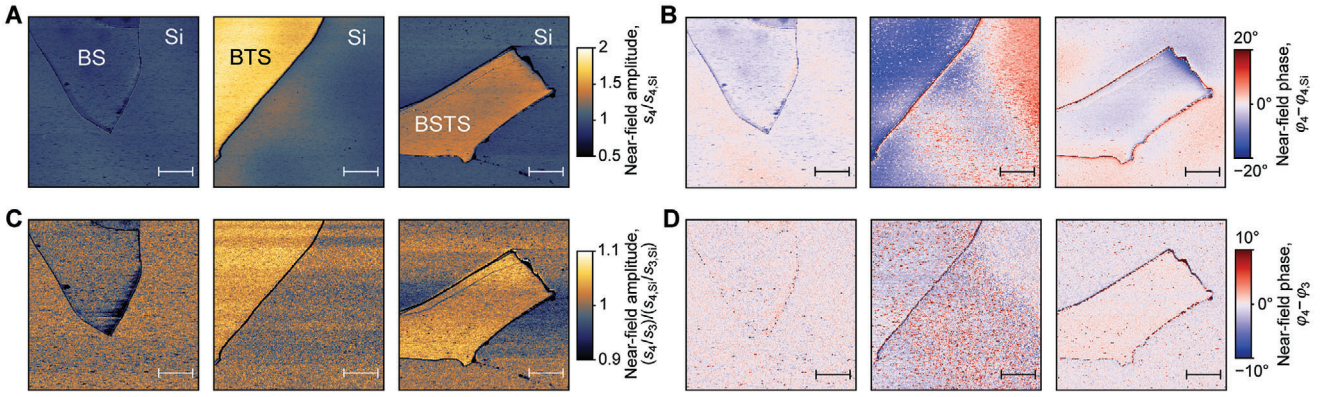

Figure 5. Spatial distributions of A) amplitude and B) phase of the near-field contrast are calculated by normalizing the near-field signal by its average over Si. C) Near-field amplitude ratio between the fourth and third demodulation harmonics normalized by that over Si, thus eliminating the effects of non-uniform tip illumination. D) Phase difference between the fourth and third demodulation harmonics of the near-field signal across the whole scan areas. All scale bars are 2 μm. Flakes thickness: BS 31 nm, BTS 188 nm, BSTS 91 nm.

between the TI flakes and Si, and in general, it is close to zero over all samples, which once again indicates the near-zero loss.

The very high permittivity of BTS and BSTS causes the nonuniform illumination of the tip as it scans over the area,[41] leading to the fluctuation of the near-field signal in Figure 5A,B. Since the nonuniform illumination proportionally contributes to all demodulation harmonics of the output signal, it can be eliminated by mapping the ratio $\sigma_{n+1}/\sigma_n = (s_{n+1}/s_n)e^{i(\varphi_{n+1}-\varphi_n)}$. The normalized amplitude ratio $(s_4/s_3)/(s_{4,Si}/s_{3,Si})$ is shown in Figure 5C, revealing the flakes edges without the signal fluctuations. Most importantly, as we discussed earlier, φ_{n+1} and φ_n reflect the near-field loss within different volumes under the tip. Thus, in a lossless material, we can expect $\varphi_{n+1} - \varphi_n = 0$. Figure 5D maps the phase difference $\varphi_4 - \varphi_3$ with much smaller signal fluctuations compared to $\varphi_4 - \varphi_{4,Si}$ (Figure 5B). Yet again, $\varphi_4 - \varphi_3 \approx 0$ across all three TI flakes, thus confirming our earlier observations.

At the same time, it has been demonstrated[46] that the mid-IR near-field phase contrast between a dielectric substrate and a 2D conductive layer should be detectable when the 2D carrier concentration exceeds $\approx 1 \times 10^{12}$ cm^{-2}, even if carrier mobility is as low as ≈ 1 cm^{2}V^{-1}s^{-1}. However, this carrier concentration is approximately two orders of magnitude smaller than theoretically predicted for any of the three TI crystals, and about an order of magnitude smaller than measured experimentally.[6] We note that bismuth chalcogenides are inert to oxygen and exhibit negligible interaction with water,[47,48] thus we exclude surface oxidation as a factor of concern. Furthermore, a recent study of BS nanobeams grown by chemical vapor deposition reported a high sensitivity of the local phase signal even to a slight variation of the generally small absorption loss in BS at mid-IR frequencies.[49]

Last but not least, we conducted near-field imaging of the edges of the TI flakes on a SiO_2/Si substrate (Figure S7, Supporting Information). We observe a near-field interference pattern typical for a propagating mode. However, the period of the pattern remains the same in every sample (Figure S7A, Supporting Information) irrespective of material and flake thickness. This implies that the near-field interference corresponds to some propagating mode in the substrate. Consequently, this means that the flakes do not screen the electric field between the SNOM nano-tip and the substrate, which is possible only if the TI bulk is dielectric and the surface states have low carrier density insufficient for screening, in agreement with previous observations. Indeed, the measured dispersion of the interference pattern over the BSTS flake indicates that it corresponds to the light line in the substrate (Figure S7B, Supporting Information). We speculate that the near-field interference corresponds to the evanescent field of light waves in the substrate launched by the sharp edges of the TI crystals which efficiently scatter the excitation beam due to their high index.

3. Conclusion

In conclusion, we studied the mid-IR electrodynamic response of three van der Waals crystals – BS, BTS, and BSTS – by several near-field probing techniques. Surprisingly, the conductive surface state was not detected by any experiment in all three TI materials. We speculate that such lossless mid-IR response can be caused by unusually low carrier concentration in the surface states, or possibly by a not-Drude-like behavior of the topological surface conductivity in the poorly investigated mid-IR regime. This puzzle demands an investigation but is out of the scope of this work.

Nevertheless, our results have significant implications for mid-IR nanophotonics: we show that these van der Waals crystals have an ultra-low loss (comparable to silicon) and ultra-high refractive index (as much as 7.5 in BTS) across a wide mid-IR frequency range from 950 to 1600 cm^{-1}. For example, as demonstrated by our experiments, exfoliated TI flakes provide a low-loss substrate for highly-confined phonon-polaritons, which generally have a much higher quality factor than plasmons. Thus, our results open new avenues for mid-IR nanophotonic applications and hint at yet-to-be-explored physical properties of certain topological insulators.

4. Experimental Section

Sample Preparation: The bulk BS, BTS, and BSTS crystals grown by the Bridgman method were commercially purchased from 2D Semiconductors USA. Mechanically exfoliated (with a low adhesion Nitto SPV224

tape) thin flakes were transferred on top of the wafer using a polydimethylsiloxane (PDMS) stamp and a manual transfer stage. Large-size bulk hBN crystal grown by the epitaxial solidification technique was also purchased from 2D Semiconductors USA, and then exfoliated and transferred in the same way as the TI flakes. The stoichiometry of the purchased TI materials has been verified by Raman spectroscopy (Figure S8, Supporting Information).

Sample Characterization: s-SNOM measurements were performed using the neaSNOM from attocube systems AG (formerly Neaspec) coupled with the tunable QCL (MIRcat, Daylight Solutions). The Pt-coated AFM tips (ARROWNCPt, Nano World) had a typical tapping frequency $\Omega \approx 270$ kHz, and the used taping amplitude was 60–70 nm in a tapping mode. The background-free interferometric signal[39] demodulated at the third and the fourth harmonics (3Ω and 4Ω) was used to generate the near-field images and analyze the near-field data. During the near-field imaging, the topography of the sample was also recorded, which was used to measure the thickness of the flakes.

Supporting Information

Supporting Information is available from the Wiley Online Library or from the author.

Acknowledgements

This research was supported by the National Research Foundation of Korea (NRF) grants funded by the Ministry of Education (NRF-2021R1I1A1A01057510) and the Ministry of Science, ICT and Future Planning (NRF-2022R1A2C2092095). This work was also supported under the framework of an international cooperation program managed by the NRF (NRF-2022K2A9A2A23000272, FY2022). N.A.M. is a VILLUM Investigator supported by Villum Fonden (Grant No. 16498). The Center for Polariton-driven Light–Matter Interactions (POLIMA) is funded by the Danish National Research Foundation (Project No. DNRF165). V.A.Z. acknowledges financial support from Villum Fonden (Grant No. 40707). This work was also supported by the BK21 FOUR Program through the NRF funded by the Ministry of Education.

Conflict of Interest

The authors declare no conflict of interest.

Author Contributions

S.G.M. and M.S.J. conceived the research concept. S.G.M. fabricated the samples, performed SNOM measurements, analyzed the data, and wrote the manuscript. J.T.H. assisted in sample preparation and SNOM measurements. V.A.Z. assisted in data analysis. N.A.M. and M.S.J. supervised the project. All authors contributed to writing the manuscript by fruitful discussions and valuable comments.

Data Availability Statement

The data that support the findings of this study are available from the corresponding author upon reasonable request.

Keywords

near-field, phonon-polaritons, topological insulators, ultra-high index, van der Waals crystals

Received: November 5, 2023
Revised: January 30, 2024
Published online:

[1] M. Z. Hasan, C. L. Kane, *Rev. Mod. Phys.* **2010**, *82*, 3045.
[2] H. Chorsi, B. Cheng, B. Zhao, J. Toudert, V. Asadchy, O. F. Shoron, S. H. Fan, R. Matsunaga, *Adv. Funct. Mater.* **2022**, *32*, 2110655.
[3] D. Hsieh, Y. Xia, D. Qian, L. Wray, F. Meier, J. H. Dil, J. Osterwalder, L. Patthey, A. V. Fedorov, H. Lin, A. Bansil, D. Grauer, Y. S. Hor, R. J. Cava, M. Z. Hasan, *Phys. Rev. Lett.* **2009**, *103*, 146401.
[4] M. Yang, H. X. Zhou, J. Wang, *Mater. Today Commun.* **2022**, *33*, 104190.
[5] A. Rogalski, *Appl. Phys. Lett.* **2023**, *123*, 230502.
[6] J. Yin, H. N. S. Krishnamoorthy, G. Adamo, A. M. Dubrovkin, Y. D. Chong, N. I. Zheludev, C. Soci, *NPG Asia Mater* **2017**, *9*, e425.
[7] H. N. S. Krishnamoorthy, A. M. Dubrovkin, G. Adamo, C. Soci, *Chem. Rev.* **2023**, *123*, 4416.
[8] J. Y. Ou, J. K. So, G. Adamo, A. Sulaev, L. Wang, N. I. Zheludev, *Nat. Commun.* **2014**, *5*, 5139.
[9] Z. J. Yue, B. Y. Cai, L. Wang, X. L. Wang, M. Gu, *Sci. Adv.* **2016**, *2*, e1501536.
[10] X. Z. Chen, D. B. Hu, R. Y. Mescall, G. J. You, D. N. Basov, Q. Dai, M. K. Liu, *Adv. Mater.* **2019**, *31*, 1804774.
[11] P. K. Venuthurumilli, X. L. Wen, V. Iyer, Y. P. Chen, X. F. Xu, *ACS Photonics* **2019**, *6*, 2492.
[12] J. S. Wu, D. N. Basov, M. M. Fogler, *Phys. Rev. B* **2015**, *92*, 205430.
[13] P. Di Pietro, M. Ortolani, O. Limaj, A. Di Gaspare, V. Giliberti, F. Giorgianni, M. Brahlek, N. Bansal, N. Koirala, S. Oh, P. Calvani, S. Lupi, *Nat. Nanotechnol.* **2013**, *8*, 556.
[14] M. Autore, H. Engelkamp, F. D'Apuzzo, A. Di Gaspare, P. Di Pietro, I. Lo Vecchia, M. Brahlek, N. Koirala, S. Oh, S. Lupi, *ACS Photonics* **2015**, *2*, 1231.
[15] T. P. Ginley, S. Law, *Adv. Opt. Mater.* **2018**, *6*, 1800113.
[16] Z. Wang, T. P. Ginley, S. V. Mambakkam, G. Chandan, Y. Y. Zhang, C. Y. Ni, S. Law, *Phys. Rev. Mater.* **2020**, *4*, 115202.
[17] E. A. A. Pogna, L. Viti, A. Politano, M. Brambilla, G. Scamarcio, M. S. Vitiello, *Nat. Commun.* **2021**, *12*, 6672.
[18] S. Chen, A. Bylinkin, Z. T. Y. Wang, M. Schnell, G. Chandan, P. N. Li, A. Y. Nikitin, S. Law, R. Hillenbrand, *Nat. Commun.* **2022**, *13*, 1374.
[19] C. P. Schmid, L. Weigl, P. Grossing, V. Junk, C. Gorini, S. Schlauderer, S. Ito, M. Meierhofer, N. Hofmann, D. Afanasiev, J. Crewse, K. A. Kokh, O. E. Tereshchenko, J. Gudde, F. Evers, J. Wilhelm, K. Richter, U. Hofer, R. Huber, *Nature* **2021**, *593*, 385.
[20] D. Singh, S. Nandi, Y. Fleger, S. Z. Cohen, T. Lewi, *Laser Photonics Rev.* **2023**, *17*, 2200841.
[21] J. Yuan, W. L. Ma, L. Zhang, Y. Lu, M. Zhao, H. L. Guo, J. Zhao, W. Z. Yu, Y. P. Zhang, K. Zhang, H. Y. Hoh, X. F. Li, K. P. Loh, S. J. Li, C. W. Qiu, Q. L. Bao, *ACS Photonics* **2017**, *4*, 3055.
[22] H. N. S. Krishnamoorthy, G. Adamo, J. Yin, V. Savinov, N. I. Zheludev, C. Soci, *Nat. Commun.* **2020**, *11*, 1692.
[23] D. Piccinotti, B. Gholipour, J. Yao, K. F. MacDonald, B. E. Hayden, N. I. Zheludev, *Adv. Mater.* **2019**, *31*, 1807083.
[24] F. Mooshammer, F. Sandner, M. A. Huber, M. Zizlsperger, H. Weigand, M. Plankl, C. Weyrich, M. Lanius, J. Kampmeier, G. Mussler, D. Grützmacher, J. L. Boland, T. L. Cocker, R. Huber, *Nano Lett.* **2018**, *18*, 7515.
[25] S. Kim, S. G. Menabde, V. W. Brar, M. S. Jang, *Adv. Opt. Mater.* **2020**, *8*, 1901194.
[26] S. G. Menabde, J. T. Heiden, J. D. Cox, N. A. Mortensen, M. S. Jang, *Nanophotonics* **2022**, *11*, 2433.
[27] H. Wang, A. Kumar, S. Dai, X. Lin, Z. Jacob, S.-H. Oh, V. Menon, E. Narimanov, Y. D. Kim, J.-P. Wang, P. Avouris, L. M. Moreno, J. Caldwell, T. Low, *Nat. Commun.* **2024**, *15*, 69.
[28] E. Galiffi, G. Carini, X. Ni, G. Alvarez-Pérez, S. Yves, E. M. Renzi, R. Nolen, S. Wasserroth, M. Wolf, P. Alonso-Gonzalez, A. Paarmann, A. Alù, *Nat. Rev. Mater.* **2024**, *9*, 9.
[29] S. Dai, Q. Ma, *Nat. Mater.* **2023**, *22*, 805.

[30] S. G. Menabde, M. S. Jang, *Nat. Nanotechnol.* **2022**, *17*, 903.
[31] S. Y. Dai, Q. Ma, Y. F. Yang, J. Rosenfeld, M. D. Goldflam, A. McLeod, Z. Y. Sun, T. I. Andersen, Z. Fei, M. K. Liu, Y. M. Shoa, K. Watanabe, T. Taniguchi, M. Thiemens, F. Keilmann, P. Jarillo-Herrero, M. M. Fogler, D. N. Basov, *Nano Lett.* **2017**, *17*, 5285.
[32] S. G. Menabde, S. Boroviks, J. Ahn, J. T. Heiden, K. Watanabe, T. Taniguchi, T. Low, D. Hwang, N. A. Mortensen, M. S. Jang, *Sci. Adv.* **2022**, *8*, eabn0627.
[33] S. G. Menabde, J. Jahng, S. Boroviks, J. Ahn, J. T. Heiden, D. Hwang, E. S. Lee, N. A. Mortensen, M. S. Jang, *Adv. Opt. Mater.* **2022**, *10*, 2201492.
[34] F. J. G. de Abajo, A. Manjavacas, *Faraday Discuss.* **2015**, *178*, 87.
[35] C. S. Tang, B. Xia, X. Q. Zou, S. Chen, H. W. Ou, L. Wang, A. Rusydi, J. X. Zhu, E. E. M. Chia, *Sci. Rep.* **2013**, *3*, 3513.
[36] N. C. Passler, A. Paarmann, *J. Opt. Soc. Am. B* **2017**, *34*, 2128.
[37] E. Shkondin, O. Takayama, M. E. A. Panah, P. Liu, P. V. Larsen, M. D. Mar, F. Jensen, A. V. Lavrinenko, *Opt. Mater. Express* **2017**, *7*, 1606.
[38] T. Taubner, R. Hillenbrand, F. Keilmann, *Appl. Phys. Lett.* **2004**, *85*, 5064.
[39] N. Ocelic, A. Huber, R. Hillenbrand, *Appl. Phys. Lett.* **2006**, *89*, 101124.
[40] L. Mester, A. A. Govyadinov, S. Chen, M. Goikoetxea, R. Hillenbrand, *Nat. Commun.* **2020**, *11*, 3359.
[41] L. Mester, A. A. Govyadinov, R. Hillenbrand, *Nanophotonics* **2022**, *11*, 377.
[42] I. Niehues, L. Mester, E. Vicentini, D. Wigger, M. Schnell, R. Hillenbrand, *Opt. Express* **2023**, *31*, 7012.
[43] A. A. Govyadinov, S. Mastel, F. Golmar, A. Chuvilin, R. S. Carney, R. Hillenbrand, *ACS Nano* **2014**, *8*, 6911.
[44] A. A. Govyadinov, I. Amenabar, F. Huth, P. S. Carney, R. Hillenbrand, *J. Phys. Chem. Lett.* **2013**, *4*, 1526.
[45] P. Aguilar-Merino, G. Alvarez-Pérez, J. Taboada-Gutiérrez, J. H. Duan, I. Prieto, L. M. Alvarez-Prado, A. Y. Nikitin, J. Martín-Sánchez, P. Alonso-González, *Nanomaterials* **2021**, *11*, 120.
[46] W. W. Luo, M. Boselli, J. M. Poumirol, I. Ardizzone, J. Teyssier, D. van Der Marel, S. Gariglio, J. M. Triscone, A. B. Kuzmenko, *Nat. Commun.* **2019**, *10*, 2774.
[47] A. Politano, M. Caputo, S. Nappini, F. Bondino, E. Magnano, Z. S. Aliev, M. B. Babanly, A. Goldoni, G. Chiarello, E. V. Chulkov, *J. Phys. Chem. C* **2014**, *118*, 21517.
[48] L. V. Yashina, J. Sánchez-Barriga, M. R. Scholz, A. A. Volykhov, A. P. Sirotina, S. N. Vera, M. E. Tamm, A. Varykhalov, D. Marchenko, G. Springholz, G. Bauer, A. Knop-Gericke, O. Rader, *ACS Nano* **2013**, *7*, 5181.
[49] S. Nandi, S. Z. Cohen, D. Singh, M. Poplinger, P. Nanikashvili, D. Naveh, T. Lewi, *Nano Lett.* **2023**, *23*, 11501.